

Long-term 4.6 μ m Variability in Brown Dwarfs and a New Technique for Identifying Brown Dwarf Binary Candidates

HUNTER BROOKS,^{1,2} J. DAVY KIRKPATRICK,² AARON M. MEISNER,³ CHRISTOPHER R. GELINO,²
DANIELLA C. BARDALEZ GAGLIUFFI,^{4,5} FEDERICO MAROCCO,² ADAM C. SCHNEIDER,^{6,7} JACQUELINE K. FAHERTY,⁵
S.L.CASEWELL,⁸ YADUKRISHNA RAGHU,⁹ MARC J. KUCHNER,¹⁰ AND THE BACKYARD WORLDS: PLANET 9 COLLABORATION

¹Department of Astronomy and Planetary Science, Northern Arizona University, Flagstaff, AZ 86011, USA

²IPAC, Mail Code 100-22, Caltech, 1200 E. California Blvd., Pasadena, CA 91125, USA

³NSF's National Optical-Infrared Astronomy Research Laboratory, 950 N. Cherry Ave., Tucson, AZ 85719, USA

⁴Physics and Astronomy Department, Amherst College, 21 Merrill Science Drive, Amherst, MA 01002, USA

⁵Department of Astrophysics, American Museum of Natural History, Central Park West at 79th Street, New York, NY 10024, USA

⁶United States Naval Observatory, Flagstaff Station, 10391 West Naval Observatory Rd., Flagstaff, AZ 86005, USA

⁷Department of Physics and Astronomy, George Mason University, MS3F3, 4400 University Drive, Fairfax, VA 22030, USA

⁸School of Physics and Astronomy, University of Leicester, University Road, Leicester, LE1 7RH, UK

⁹Backyard Worlds: Planet 9

¹⁰NASA Goddard Space Flight Center, Exoplanets and Stellar Astrophysics Laboratory, Code 667, Greenbelt, MD 20771, USA

ABSTRACT

Using a sample of 361 nearby brown dwarfs, we have searched for 4.6 μ m variability indicative of large-scale rotational modulations or large-scale long-term changes on timescales of over 10 years. Our findings show no statistically significant variability in *Spitzer* ch2 or *WISE* W2 photometry. For *Spitzer* the ch2 1σ limits are ~ 8 mmag for objects at 11.5 mag and ~ 22 mmag for objects at 16 mag. This corresponds to no variability above 4.5% at 11.5 mag and 12.5% at 16 mag. We conclude that highly variable brown dwarfs, at least two previously published examples of which have been shown to have 4.6 μ m variability above 80 mmag, are very rare. While analyzing the data, we also developed a new technique for identifying brown dwarfs binary candidates in *Spitzer* data. We find that known binaries have IRAC ch2 PRF (point response function) flux measurements that are consistently dimmer than aperture flux measurements. We have identified 59 objects that exhibit such PRF versus apertures flux differences and are thus excellent binary brown dwarf candidates.

Keywords: Brown Dwarfs, Low-Mass Stars, Variability, Binaries, Subdwarfs

1. INTRODUCTION

Brown dwarfs have similar chemical composition and size to large gaseous planets, indicating that brown dwarfs have the potential for cloud bands and large surface storms, like that of the Great Red Spot on Jupiter. It has been found that some brown dwarfs exhibit variability over short periods of a couple of hours to a few days, first reported in Bailer-Jones & Mundt (1999) and Kolb & Baraffe (1999). Artigau et al. (2009) and Yang et al. (2016) found variability as high as 14-420 mmag, mostly in the *J*, *H*, and *K* bands over several rotational periods. This is a result of inhomogeneities in the brown dwarf's cloud bands or local storms, which induces observed variability as the object rotates. However, none of these papers explore long-term variability over timescales of years. Additionally, we might expect

stellar flares in the warmest brown dwarfs as a result of their similarities to low-mass stars (Gizis et al. 2017, Ducrot et al. 2020).

The goal of this paper is to examine long-term variability, on years to decade timescales, at $\sim 4.6\mu$ m for a large brown dwarf sample. This would not only be sensitive to rotationally modulated variability due to inhomogeneity over the surface, but would also be sensitive to long-term global changes in the atmosphere.

While examining variability, we developed a new technique for identifying brown dwarf binary candidates in *Spitzer* data. Our *Spitzer* reductions measure both the aperture and point response function-fit (hereafter, PRF-fit) fluxes. If the PRF-fit fluxes are consistently dimmer than the aperture measurements, then it may be indicative of a binary brown dwarf system. We

demonstrate this with known binaries and background-contaminated objects.

In §2 we discuss expectations of variability based on previous research. We then discuss the data acquisition and reduction in §3 and its analysis in §4. Long-term variability is explored in §5, while the new technique for discovering brown dwarf binary candidates is discussed in §6. The results from these two sections are then compared to what was previously known about brown dwarf variability and binarity in §7.

2. VARIABILITY EXPECTATIONS

Most previous papers on brown dwarf variability have focused on hemisphere-to-hemisphere inhomogeneity. As a result of brown dwarfs having a range of rotational periods from about an hour to a few weeks (Tannock et al. 2021, Luhman 2012), these studies have only concentrated on a few-day to few-week timescale. Some of these studies have repeated this analysis on return trips to look for anomalies on the surface of brown dwarfs that might change many rotational periods in the future (Apai et al. 2017).

Studies such as Kellogg et al. (2017), Radigan et al. (2012), Radigan et al. (2014a), and Radigan (2014b) between 0.9-2.5 μm and Vos et al. (2022) and Yang et al. (2016) between 3.6-4.5 μm found variability in the L/T dwarf transition but did not sample the entire brown dwarf spectral range. Additional studies (Metchev et al. 2015 and Cushing et al. 2016) found that large variations of >2% in *Spitzer*/IRAC ch1 ($\sim 3.6\mu\text{m}$) and ch2 ($\sim 4.5\mu\text{m}$) exist across L/T/Y spectral types. It has been shown that large variations occur in the *J* ($\sim 1.25\mu\text{m}$) and *K/K_s* ($\sim 2.2\mu\text{m}$) bands, sometimes as large as 420mmag in *K_s* (Artigau et al. 2009). Studies at r-band ($\sim 0.658\mu\text{m}$) for M and L dwarfs found that $\sim 50\%$ vary at a level of >2% (Artigau 2018).

Brown dwarf variability is believed to be caused by a variety of different physical phenomena. The most explored and discussed explanation is that brown dwarfs have a mixture of dusty clouds and hazes (e.g. Marley et al. 2013 and Tsuji 2005). SIMP J013656.57+093347.3 is believed to have 75% of its surface covered by dusty clouds based on its *K_s* to *J* variability ratio, $\frac{\Delta K_s}{\Delta J}$ (Artigau et al. 2009). An alternative idea is that variability is caused by differentially rotating cloud bands. Some cloud bands may appear more optically thin, depending on the filter used. This idea is explored in Yang et al. (2016), where six brown dwarfs were observed to have variability on the scale of a few percent. This variability was linked to differential cloud rotation and atmospheric optical depth, causing inhomogeneities in longitude.

Another scenario is local storms that can be seen on the top of an object’s atmosphere, similar to the Great Red Spot on Jupiter. Jupiter and brown dwarfs have been juxtaposed multiple times throughout the history of brown dwarfs studies. Gelino & Marley (2000) explore the similarities that the gas giants of our solar system could have with brown dwarfs. As a storm rotates or increases/decreases in size, it could lead to variability seen in an unresolved disk. Gelino & Marley (2000) predicted that an unresolved storm similar to Jupiter’s Great Red Spot would create variability on the order of 0.2 mag at 4.78 μm but only 0.04 mag at 0.410 μm . Ge et al. (2019) found that Jupiter exhibits peak-to-peak variability upwards of 20% at 5 μm , which is where this variability is the greatest, indicating that brown dwarfs may exhibit such behavior and that using the *WISE* W2 band would be an excellent band in which to search for such variability in brown dwarfs.

Our study uses a different approach than previous studies of brown dwarf variability, such as Metchev et al. (2015) who used *Spitzer*/IRAC’s sweet spot for which corrections for the pixel phase effect (Deming et al. 2015) enables extremely high levels of photometric precision. Such studies are thus sensitive to small amplitude variability (>0.2% for 3 to 5 μm) at short timescales (typically <20 hours). While studies of variability over longer time baselines of several months have been performed (e.g., Yang et al. 2016), an investigation of substellar object variability over several year time baselines has yet to be attempted. Because our observations are randomly sampled over several years, we expect significant coverage of all hemispheres, allowing for an investigation of large-amplitude variability.

3. PHOTOMETRY

3.1. *Spitzer*/IRAC Channel 2

The photometry used in this work is derived from the *Spitzer* observations (IRSA 2022) used to compute the trigonometric parallaxes of 361 L, T, and Y dwarfs in Kirkpatrick et al. (2021), covering a long time baseline (Figure 1). This long time baseline, spanning upwards of seventeen years, provides an excellent dataset with which to study brown dwarfs at their peak wavelengths over a timescale that has never been explored before. The photometry comes from *Spitzer*’s Infrared Array Camera (hereafter, *Spitzer*/IRAC; Fazio et al. 2004), which, during the cryogenic mission, was capable of observing at ch1 ($\sim 3.6\mu\text{m}$), ch2 ($\sim 4.6\mu\text{m}$), ch3 ($\sim 5.8\mu\text{m}$), and ch4 ($\sim 8.0\mu\text{m}$) bands (Werner et al. 2004). Of these four, the one that was used is *Spitzer* ch2, as this is the band in which brown dwarfs are brightest (Mainzer et al. 2011).

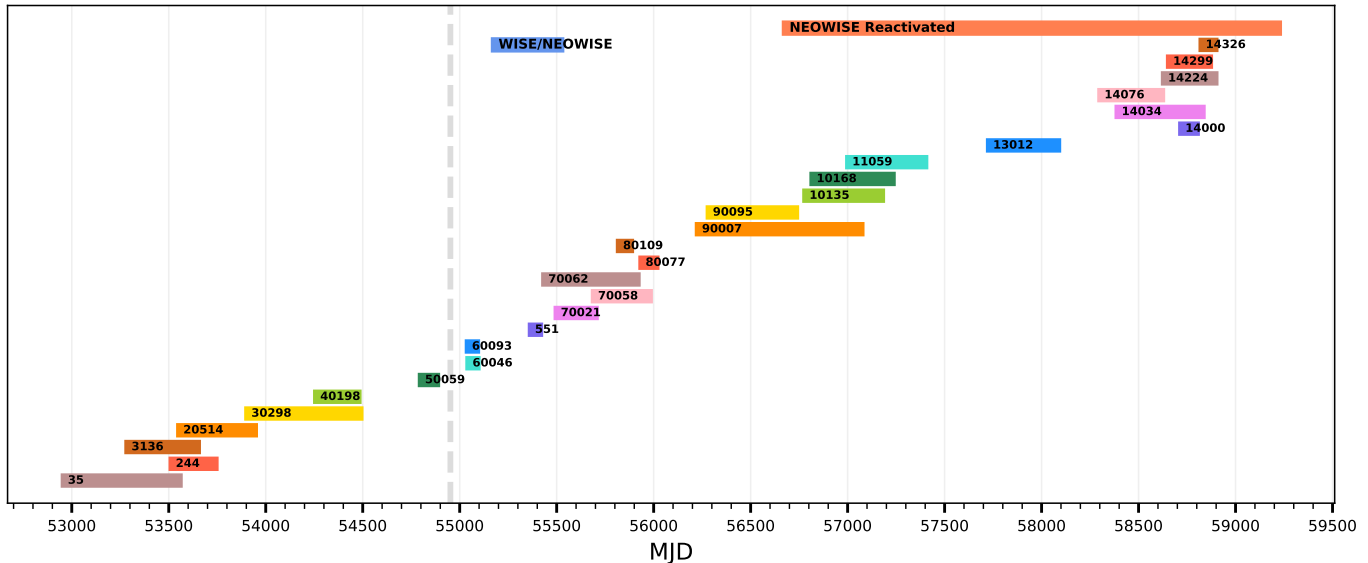


Figure 1. Observation windows of both the *Spitzer* and *WISE* data sets used in this paper. The *Spitzer* program number (black numbers) and the time span that it surveyed are shown by the rainbow lines if the time period is only a handful of nights (Table 3 in Kirkpatrick et al. 2021). The *WISE* timescale is shown by the top two lines that include “WISE/NEOWISE” and “NEOWISE Reactivation” (Mainzer et al. 2014). Finally, the light-gray dashed vertical line marks the transition from the *Spitzer* cryogenic mission to the warm mission. For example, 53000 MJD is December 27th, 2003 and 59500 MJD is October 13th, 2021.

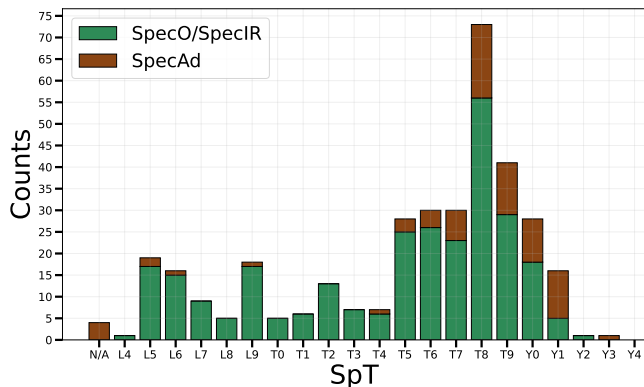


Figure 2. The spectral type distribution of the 361 objects from Kirkpatrick et al. (2021). Optical spectral types (SpecO) are used for L dwarfs and infrared types (SpecIR) are used for T and Y dwarfs. For objects without confirmed spectral types, we take the types estimated using available photometry (SpecAd).

Spitzer’s cryogenic mission observed only 14 of the 361 objects in our sample. However, every object includes *Spitzer* warm mission ch2 data, and most have a time baseline of >10 years.

The spectral type distribution for these 361 brown dwarfs is seen in Figure 2. These spectral types come from Kirkpatrick et al. (2021) where objects that have optical and infrared spectra are marked as “SpecO/SpecIR” and objects that have spectral classifications based on colors are marked with “SpecAd”.

Most objects are at distances <20 pc, which makes them the brightest members of their class. Hence, the photometric uncertainties will be as low as possible, allowing us the best chance to detect variability for these classes. Moreover, the majority of these objects were observed for several years and multiple times a year, meaning that each object will have an abundance of data points.

Figure 3a shows the number of Astronomical Observation Requests (hereafter, AOR), N_{spitzer} , for all 361 objects. Most objects have 6-16 AORs. However, many objects have >16 AORs and these will have the most data-rich light curves.

3.2. WISE W2

To provide additional $4.6\mu\text{m}$ data, NASA’s *Wide-field Infrared Survey Explorer* (hereafter, *WISE*; Wright et al. 2010) and *Near-Earth Object WISE* (hereafter, *NEOWISE*; Mainzer et al. 2011) W2 photometry was considered. As Figure 15 of Kirkpatrick et al. (2021) shows, *Spitzer* ch2 and *WISE* W2 filter bandpasses for brown dwarfs can be interchanged. *WISE* data were obtained by cross-matching our objects with the unTimely Catalog (Meisner et al. 2022), which contains detections from *WISE/NEOWISE* W2 coadds. The unTimely Catalog contains time-series W1 and W2 photometry from the beginning of the *WISE* mission to the most current publicly released *NEOWISE* data. The *WISE* and *NEOWISE* timescales can be seen at the top of Figure

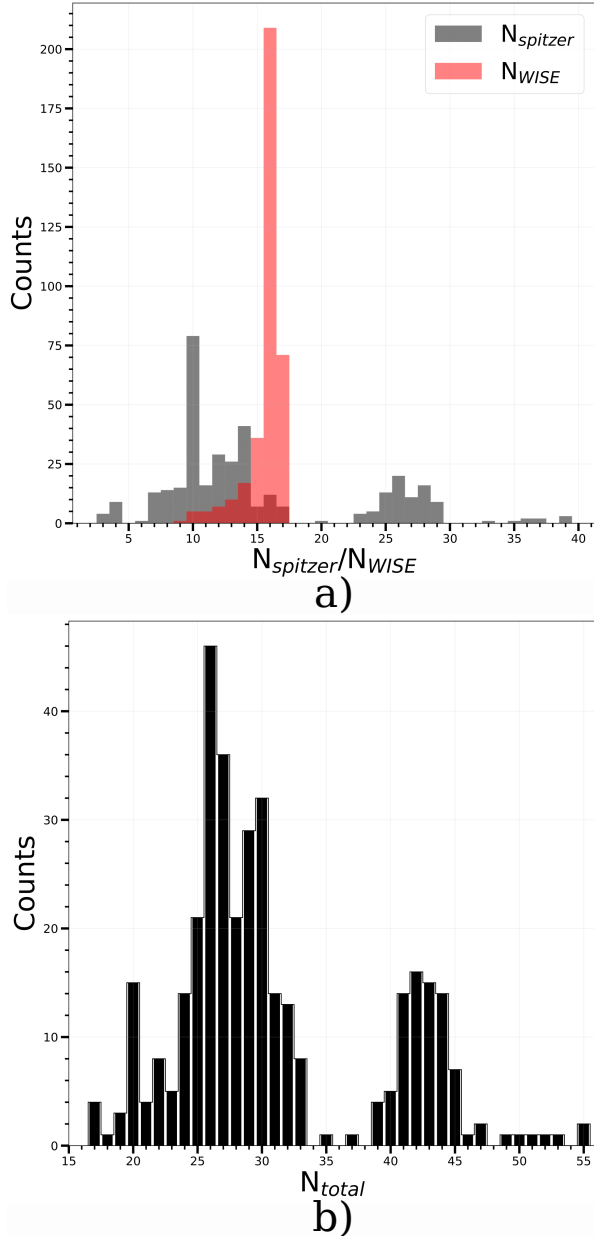


Figure 3. Subplot (a) displays a histogram of the number of AORs ($N_{spitzer}$) for each object in our sample of 361 brown dwarfs, displayed in gray. The distribution is multimodal, though most objects have between 6 and 16 AORs. The red distribution of subplot (a) is a histogram of the number of unTimely detections found for each object (N_{WISE}). Subplot (b) is a histogram of the total number of points for each object where $N_{total} = N_{spitzer} + N_{WISE}$.

1. The unTimely Catalog also contains W1 photometry over multiple epochs; this photometry could be explored for variability in future research.

Figure 3a shows the distribution of the number of unTimely detections, N_{WISE} , per object. There is much less variation compared to $N_{spitzer}$ as a result

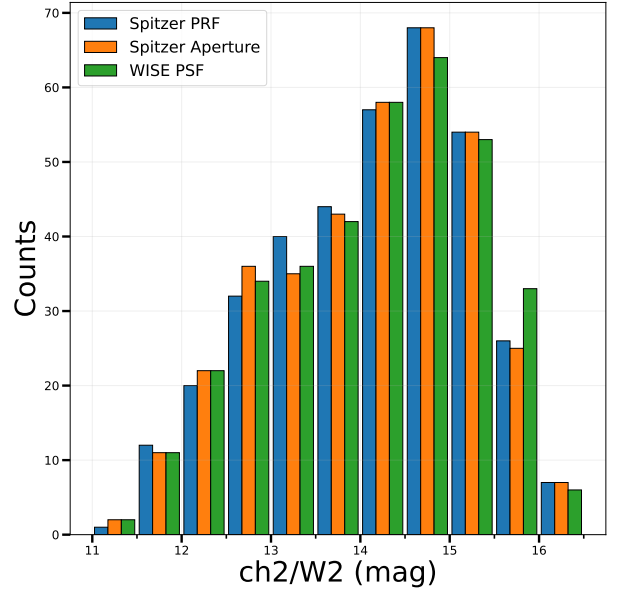


Figure 4. A histogram of the total number of Spitzer PRF (blue), Spitzer aperture (orange), and WISE Point Spread Function (green) average magnitudes for each 0.5mag wide bin.

of *WISE/NEOWISE* covering the whole sky every six months. Theoretically, every object should have 16 unTimely detections for each of the 16 sky passes made from classic *WISE* up through *NEOWISE* year 7. However, some objects have N_{WISE} values of <16 because of background contamination problems. Due to the fact that the *WISE* spacecraft precesses, some objects will have N_{WISE} values of 17 because in *NEOWISE* year 7 a portion of the sky already has its 17th coverage. The distribution of the number of points per object, combining $N_{spitzer}$ and N_{WISE} , can be seen in Figure 3b. Figure 4 displays the distribution for each photometry measurement per magnitude interval. Lastly, Figure 5 shows the distribution of *Spitzer* and unTimely points per MJD interval. We can see that the number of points per unit time increases with time.

4. UNDERSTANDING THE PHOTOMETRY

An object's median *Spitzer* ch2 flux and its standard deviation were calculated for a single AOR by taking the median of the measured flux in all the dithers for that particular AOR. The magnitudes were calculated using these formulas:

$$ch2_{aperture} = 2.5 \times \log_{10} \left(\frac{F_0}{F_{ap} \times C_{ap}} \right) \quad (1)$$

$$ch2_{PRF} = 2.5 \times \log_{10} \left(\frac{F_0}{F_{PRF} \times C_{PRF}} \right) \quad (2)$$

where $ch2_{aperture}$ is the aperture magnitude, $ch2_{PRF}$ is the PRF-fit magnitude, F_0 is the flux at zero magnitude (179700000 μJy , Table 4.2 of the *Spitzer*/IRAC Handbook¹), F_{ap} is the measured aperture flux in μJy from the MOPEX/APEX output (described below), F_{PRF} is the measured PRF-fit flux in μJy from the same output, C_{ap} is the aperture correction (Table 4.8 of the *Spitzer*/IRAC Handbook), and C_{PRF} is the PRF-fit correction (Table C.1 of the *Spitzer*/IRAC Handbook). This median technique was done to help us mitigate dithers that were affected by cosmic ray hits.

For the unTimely data points, the only measurement that is offered in the catalog is a Point Spread Function-fit (hereafter, PSF-fit; Schlafly et al. 2019), which is analogous to the *Spitzer* PRF-fit. Flux measurements were obtained directly from the catalog because Schlafly, Meisner, & Green (2019) calculated the flux and its uncertainties within the code. The magnitudes and their uncertainties were calculated using the formula: $\text{mag}_{WISE} = 22.5 - 2.5 \times \log_{10}(F_{WISE})$ (Schlafly, Meisner, & Green 2019).

Our *Spitzer* ch2 data were reduced in Kirkpatrick et al. (2021) using the MOPEX/APEX code (Makovoz et al. 2006). Aperture photometry counts all the flux within a circle of fixed radius. For this study, the aperture radius used is $4''.8$. For background subtraction, the flux in a concentric annulus is medianed, and that value is subtracted off the aperture measurement to reveal the true target flux. The annulus has an inner radius of $28''.8$ and an outer radius of $48''.0$ (*Spitzer*/IRAC Handbook²). The second photometry method is to perform a PRF fit (Hora et al. 2012), which approximates the 3 parameter (x, y, and flux) distribution of our target flux to a known 3 parameter shape of a point source. The aperture and PRF-fit measurements were used to verify any variability seen, because if a variable point is seen in both measurements, it suggests that it is real and not an artifact of processing. For example, the aperture measurement is susceptible to cosmic ray hits, while the PRF-fit photometry ideally can remove this contamination.

To further test the consistency of the *Spitzer* PRF-fit $ch2_{PRF}$ measurements with those of the unTimely PSF-fit, we plotted the difference between the average $ch2_{PRF}$ and the average $W2_{PSF}$ for each object. This is plotted against spectral type in Figure 6. The trend hovers around 0 for objects before T8, which supports the com-

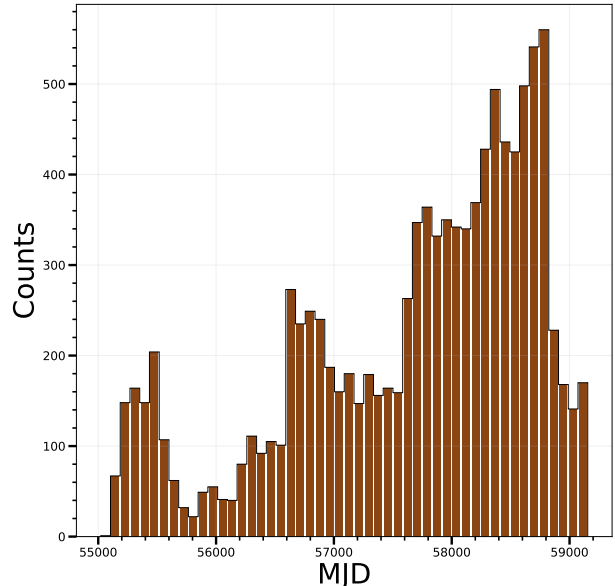


Figure 5. A histogram of the number of points for each MJD interval for both *Spitzer* and *WISE*. Each bin is 82 days each.

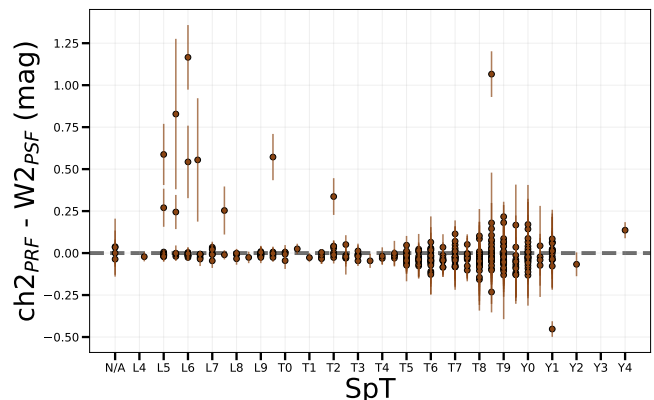


Figure 6. Comparison of spectral type versus the difference between the *Spitzer* $ch2_{PRF}$ median and the unTimely $W2_{PSF}$ median. The large outliers are a result of the *Spitzer* code trying to passively deblend the point source (further discussed in §6.1). Otherwise, we see a general trend in which the *Spitzer* $ch2$ and unTimely $W2$ photometry match extremely well, consistent with Figure 15 from Kirkpatrick et al. (2021).

patibility of the *Spitzer*/IRAC $ch2$ magnitudes and the *WISE*/unTimely $W2$ magnitudes. Objects later than T8 have a considerable amount of scatter as a result of these objects having poor S/N in $W2$. Outliers earlier than spectral type T8 on this plot are a result of blending in *Spitzer* or *WISE* caused by background contamination or possibly binarity, as further discussed in §6.

An important statistic to consider is the χ^2 value for the *Spitzer* PRF-fit. The cause of a high χ^2 is that the

¹ https://irsa.ipac.caltech.edu/data/SPITZER/docs/irac/iracinstrumenthandbook/IRAC_Instrument_Handbook.pdf

² https://irsa.ipac.caltech.edu/data/SPITZER/docs/irac/iracinstrumenthandbook/IRAC_Instrument_Handbook.pdf

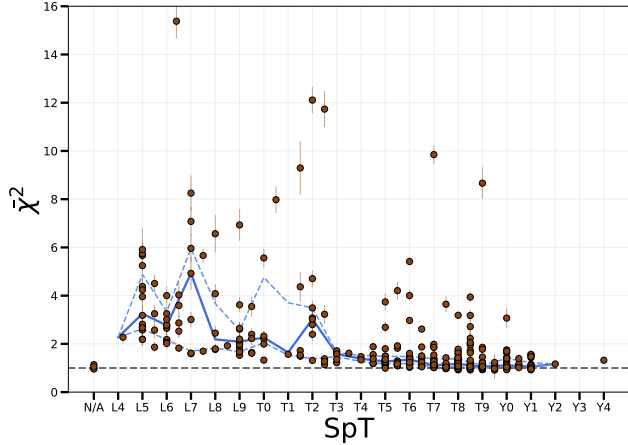


Figure 7. Comparison of the spectral type (Figure 3 sub-plot a) to the averaged χ^2 (for the ch2_{PRF} fit) for each object. The solid blue line is the median for each spectral type, while the dashed light blue lines are the 25th and 75th percentile for each spectral type. Note the large outliers on this plot, most of which were identified as possible binary candidates (further discussed in §6.1). Lastly, one object, 2MASS J22551861–5713056 (Kendall et al. 2007), which has a χ^2 value of ~ 68 , is not shown on this plot. This is a known brown dwarf binary (Reid et al. 2008).

MOPEX ch2 PRF was a poor fit to the data. In Figure 7 we compare spectral type to the averaged χ^2 value. The object’s AOR χ^2 value was calculated by performing a weighted average of all the dithers, and then the overall χ^2 was computed using a weighted average of all the AORs (the weight for these averages are the inverse variance for the photometry). The solid blue line in Figure 7 is the median for each spectral type, with the dashed light blue lines showing the lower and upper quartiles Q1 (25%) and Q3 (75%). Outliers are discussed further in §6.

5. VARIABILITY RESULTS

Now that the photometry has been analyzed, we can discuss our definition of variability. To formally define variability, we require that there are points lying $>3\sigma$ away from the median value. A 3σ requirement means that we would expect only one object in a sample of 361 independent objects to show such an excursion by chance. This $>3\sigma$ requirement searches for variability for each photometry type separately: $\text{ch2}_{aperture}$, ch2_{PRF} , and $W2_{PSF}$. We found that 24 of our 361 objects have such variability.

We found that the variability for all 24 objects is a result of a non-physical property of the brown dwarf. All 24 objects are listed in Table 1. The most common cause of $W2_{PSF}$ variability is contamination from a background source that the object was blended with

in one or more epochs. All objects with $\text{ch2}_{aperture}$ variability have a single AOR that is bombarded with cosmic ray hits in all but a few dithers. With all 24 objects being labeled as false, we find 0 out of 361 objects with true long-term variability. We further discuss this result in §7.1. The complete figure set of light curves (361 images) is available in the online journal. An example from this figure set can be seen in Figure 8.

Fig. Set 8. Light curves for the 361 objects

6. NEW TECHNIQUE FOR IDENTIFYING BINARY BROWN DWARF CANDIDATES

As discussed in §4 we use two different types of flux measurements for the *Spitzer* ch2 photometry, both aperture and PRF-fit. A disadvantage of the aperture magnitude is that it can become cross contaminated from a secondary component, background source, or cosmic ray hit. The *Spitzer* ch2 PRF-fit code, on the other hand, can attempt to fit the secondary, remove the background source, or ignore the cosmic ray to better estimate the true apparent magnitude for the object. However, the PRF-fit magnitude can be biased if the object is a partly resolved physical binary (within the MOPEX FWHM; later discussed in §7.2) or a blend with a distant stellar object or extragalactic source.

Our binary identification technique is a close variant of the widely used star-galaxy separation technique that interprets an excess of aperture flux relative to PSF flux as an indication of resolved rather than pointlike morphology. Such an approach has been used by major optical surveys, including Pan-STARRS (e.g., Schlafly et al. 2012).

Within *Spitzer*’s ch2 PRF fitting code, there is a procedure called “passive deblending”, in which the code tries to separate what is believed to be two, or more, sources and then tries to fit multiple PRFs to the detection (Makovoz & Marleau 2005). Once multiple PRFs are fit to the detection, those are subtracted to get uncertainties, χ^2 , and the S/N to compare to a single PRF-fit. MOPEX then determines whether the single or multiple PRF-fit performed better. If more than two components are fit simultaneously, the flux measurements can be drastically off (Makovoz & Marleau 2005). The code, therefore, only tries to fit one other component. This is done in a 7×7 pixel area, $7''.67 \times 7''.67$, compared to a single PRF fit in a 5×5 pixel area, $5''.48 \times 5''.48$. Passive deblending was enabled for all of the 361 brown dwarfs (Kirpatrick et al. 2021), and we used whichever fit had better metrics.

6.1. Aperture-PRF Comparison Technique

For some of the 361 objects, a trend is seen when comparing $\text{ch2}_{aperture}$ to ch2_{PRF} . Specifically, all the PRF

Table 1. Objects With Spurious Variability

Object Name	RA (Deg)	Dec (Deg)	Dataset	Note
WISE J003110.04+574936.3	7.79433	57.826773	W2 _{PSF}	Blended with Background Source
WISE J003231.09−494651.4	8.128736	−49.782059	W2 _{PSF}	Blended with Background Source
WISEP J015010.86+382724.3	27.546953	38.456528	W2 _{PSF}	Blended with Background Source
WISEPA J031325.96+780744.2	48.359129	78.129099	ch2 _{PRF}	Blended with Background Source
WISE J032504.33−504400.3	51.268182	−50.733501	W2 _{PSF}	Blended with Background Source
SDSSp J033035.13−002534.5	52.64629	−0.42628	W2 _{PSF}	Blended with Background Source
2MASS J04210718−6306022	65.281665	−63.099437	W2 _{PSF}	Blended with Background Source
WISE J064723.23−623235.5	101.84721	−62.542746	ch2 _{PRF}	Cosmic Ray Affects 1 Epoch
WISE J071322.55−291751.9	108.34441	−29.298264	W2 _{PSF}	Blended with Background Source
WISE J103907.73−160002.9	159.78173	−16.001139	ch2 _{PRF}	Cosmic Ray Affects 1 Epoch
WISE J112438.12−042149.7	171.15781	−4.363732	W2 _{PSF}	Blended with Background Source
WISEA J114156.67−332635.5	175.48445	−33.443475	ch2 _{PRF} /W2 _{PSF}	Blended with Background Source
WISEPC J151906.64+700931.5	229.77879	70.157919	ch2 _{PRF} /W2 _{PSF}	Blended with Background Source
CWISEP J160835.01−244244.7	242.14633	−24.712494	W2 _{PSF}	Blended with Background Source
WISEPA J171104.60+350036.8	257.76888	35.010238	ch2 _{PRF}	Cosmic Ray Affects 1 Epoch
WISE J174303.71+421150.0	265.76558	42.196369	W2 _{PSF}	Blended with Background Source
WISE J192841.35+235604.9	292.17202	23.93489	ch2 _{PRF}	Blended with Background Source
WISE J195500.42−254013.9	298.7526	−25.671162	ch2 _{PRF}	Cosmic Ray Affects 1 Epoch
WISEPA J195905.66−333833.7	299.77339	−33.642956	ch2 _{aperture}	Cosmic Ray Affects 1 Epoch
WISE J201546.27+664645.1	303.94207	66.779688	ch2 _{PRF}	Blended with Background Source
CWISEP J210007.87−293139.8	315.03349	−29.52782	W2 _{PSF}	Blended with Background Source
WISEPA J231336.40−803700.3	348.40273	−80.616879	ch2 _{PRF}	Blended with Background Source
WISE J235716.49+122741.8	359.31997	12.459123	ch2 _{aperture}	Cosmic Ray Affects 1 Epoch

points are dimmer than the aperture measurements. Of 361 objects, 126 (35%) show this effect. A possibility is that a blended secondary component, which is being appropriately measured in the aperture’s radius, causes a poor PRF fit measuring only the primary component. (The unTimely data were not used in this test because there is only a PSF fit with no corresponding aperture measurement.)

The 126 objects showing this trend have been divided into four different classes:

- Class 0: Includes only those objects for which passive deblending in the *Spitzer* PRF-fit photometry was triggered 100% of the time and $N_{spitzer} > 5$ (for statistical robustness). This class includes 16 objects.
- Class 1: Includes objects for which $\tilde{ch}2_{aperture} + \sigma_{\tilde{ch}2_{aperture}} < \tilde{ch}2_{PRF} - \sigma_{\tilde{ch}2_{PRF}}$ and the three rules below apply. This class includes 11 objects.
- Class 2: Includes objects for which $\tilde{ch}2_{aperture} < \tilde{ch}2_{PRF} - \sigma_{\tilde{ch}2_{PRF}}$ and the three rules below apply. This class includes 35 objects.
- Class 3: Includes objects for which the Class 1 and 2 restriction on $\tilde{ch}2_{aperture}$ do not apply, but the

three rules below are still met. This class includes 64 objects.

For an object to fall in Class 1-3, it must have the following three characteristics:

- *Spitzer* aperture magnitude brighter than its PRF-fit magnitude at every epoch.
- $N_{spitzer} > 5$ (again for statistical robustness)
- Passive deblending must have been triggered less than 100% of the time.

The subplots in Figure 8 show examples of Classes 1, 2, and 3.

These four classes were considered for binary candidacy because a possible secondary could be affecting the flux measurements. This method has the potential to discover physical brown dwarf binaries with the components having the same distance, metallicity, and age. Figure 9 shows various imaging of WISE J022623.98−021142.8 (Kirkpatrick et al. 2011), which is known to have a secondary component. We see that the binary is clearly separated in *Keck*/NIRC2 *J* (top panel; Gelino 2012), while in *Spitzer*/IRAC ch2 (middle panel; Kirkpatrick et al. 2021) and *WISE*/unTimely W2

(bottom panel; Meisner et al. 2022) it is blended. Note that the secondary is significantly redder in J -ch2 than the primary. Kirkpatrick et al. (2021) shows that for objects later than T5, the J -ch2 color quickly changes towards very large values. Figure 14d of the same paper shows that the decrease of M_{ch2} with spectral type is less drastic. One can imagine a system like WISE J022623.98–021142.8 for which the secondary is even colder. In this case, the ground-based J -band image might not have the sensitivity to detect the companion, but at the $4.6\mu\text{m}$ wavelength of *Spitzer*, the presence of the companion could be detected. Thus, this technique has the potential to identify new binaries in which the companion objects are too low in temperature to be found in ground-based, J -band follow-up. Additionally, it also provides a priority target list of nearby brown dwarfs that may not yet have seen any high-resolution imaging follow-up. For example, if a late-T or early-Y dwarf has a secondary candidate around it, there is a possibility it would be the first ever mid-late Y dwarf found.

For Figure 6, which compares $ch2_{PRF}$ and $W2_{PSF}$, we find that all the outliers were marked as Class 0. As illustrated in Figure 9, the poorer resolution of the *WISE* data blends the secondary more thoroughly with the primary, meaning that the *WISE* PSF fit is more successful at capturing the light of both components. In Figure 7, all but one outlier (mentioned in the caption) are identified as Class 1. This is because Class 1 objects are blended enough that a single PRF fit, though still poor, is not bad enough to trigger passive deblending, which would have made them Class 0 objects. Note that Classes 1-3 are numbered this way in order of the severity of the difference between the aperture and PRF-fit measurements. Class 0's name results from its being a unique class compared to the rest.

6.2. Possible Contamination by Subdwarfs

The spectral energy distributions of subdwarfs show drastic differences compared to normal dwarfs within the wavelength ranges where they have been observed (Lodieu et al. 2019). Subdwarfs are the metal-poor counterparts to normal metallicity brown dwarfs (Lépine et al. 2003). This could affect how the point source looks on the detector. If there are large absorption bands in $ch2/W2$ that are drastically altering the effective wavelength through this bandpass, it would, because of the wavelength dependence of the MOPEX FWHM, change the full width half maximum value of the PRF. This difference between the expected PRF fit and the true PRF fit of a subdwarf would result in a high χ^2 value. This is partly supported by the fact that one object in

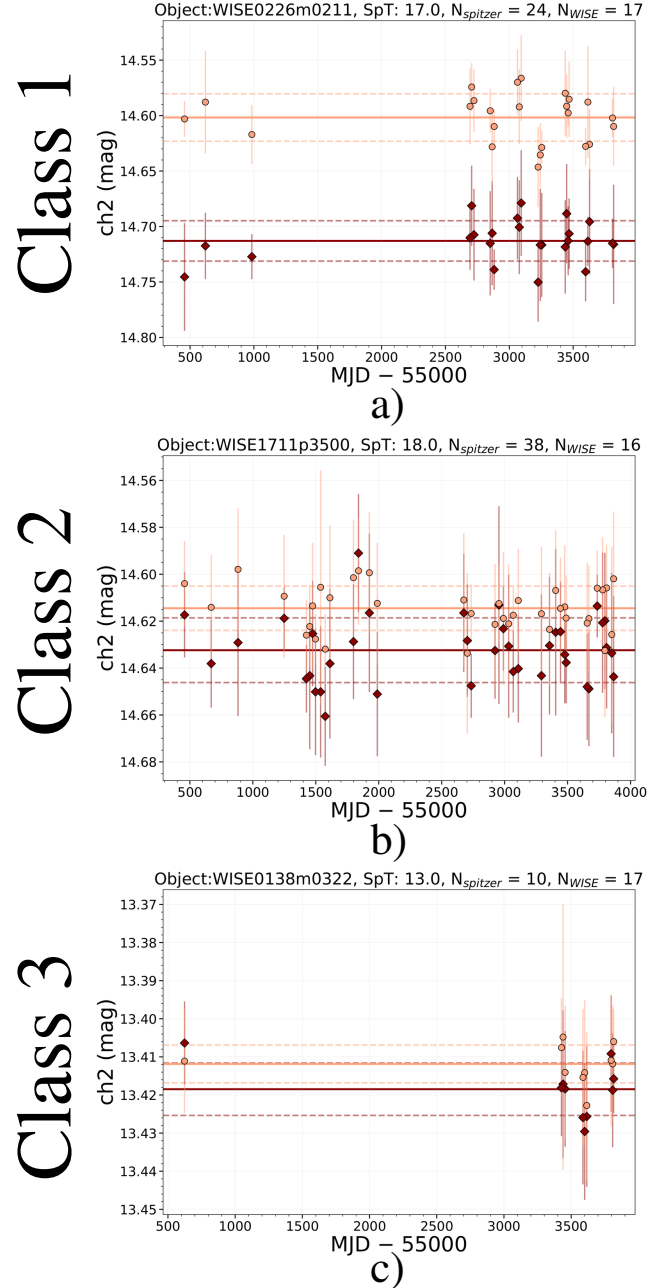


Figure 8. Light curves of three example objects. The x-axis is Modified Julian Date (MJD), with the y-axis being $ch2_{aperture}$ (orange circles) and $ch2_{PRF}$ (red diamonds). The objects in this plot are WISEPA J022623.98–021142.8 (subplot a), WISEPA J171104.60+350036.8 (subplot b), and WISEPC J013836.59–032221.2 (subplot c). The solid horizontal line is the median for each type of measurement, while the dashed lines show $\pm 1\sigma$. All of these objects are known brown dwarf binaries. For Class 1 the lower orange dashed line lies brighter than the upper red dashed line. For Class 2 the orange solid line lies brighter than the upper red dashed line. In Class 3, the solid orange line falls below the upper red dashed line. For all three classes the other three rules, discussed in the text, also apply.

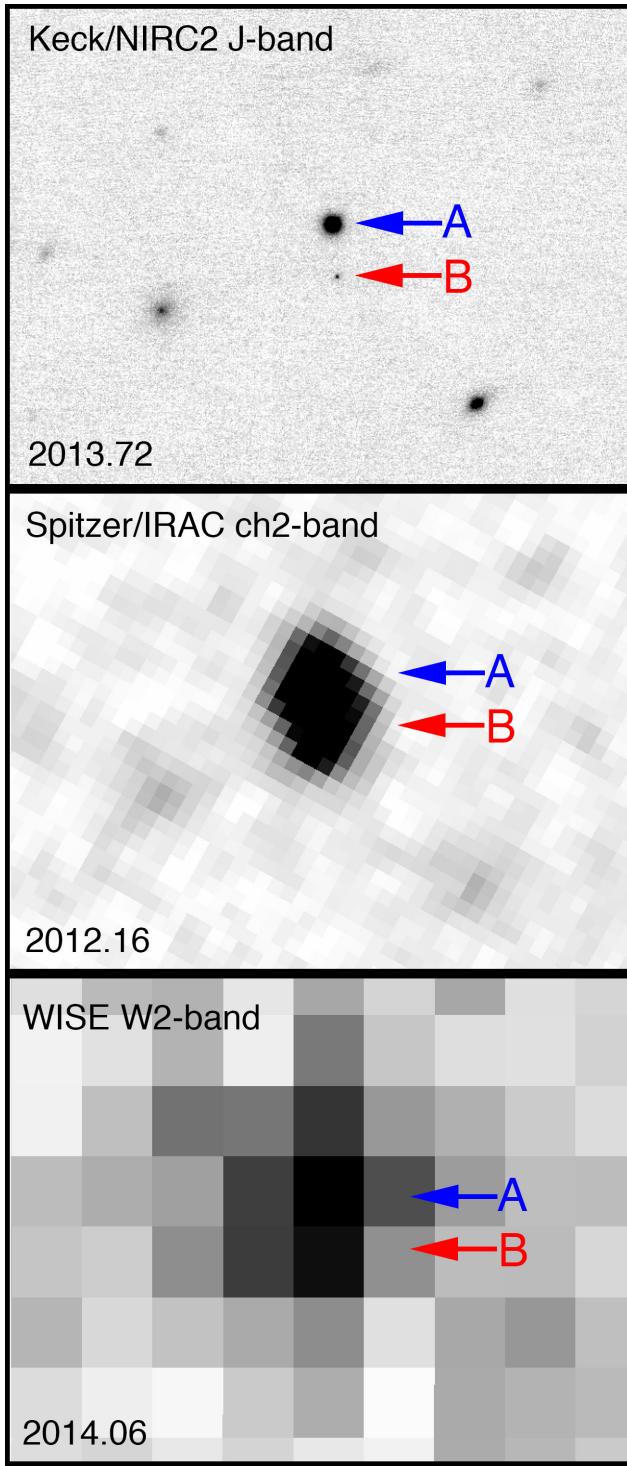


Figure 9. Images at different angular resolutions for the same object, WISE J022623.98–021142.8 (Kirkpatrick et al. 2011). *Keck*/NIRC2 *J* (top panel; Gelino 2012), *Spitzer*/IRAC ch2 (middle panel; Kirkpatrick et al. 2021), and *WISE*/unWISE W2 (bottom panel; Lang 2014). The panels are 20×30 arcsec with up being north and left being east. The primary is labeled with a blue “A”, while the secondary is a red “B”. See §6.1 for details.

Class 3, 2MASS J06453153–6646120 (Kirkpatrick et al. 2010), is an L subdwarf. We have compared a “LOWZ”³ (Meisner et al. 2021) spectral model of $Z=-1.5$ and $T_{eff}=1300\text{K}$ to a solar-metallicity model at the same temperature. For the low-metallicity model, there is relatively more flux in the blue half of the W2 band compared to the solar-metallicity model. Based on this effect, we would expect a small change in the PRF width for the low-metallicity object, likely not large enough to support the hypothesis above. However, the models at these low-metallicities are completely untested in this wavelength regime. This effect can not be currently quantified because of the lack of observational spectra for subdwarfs at $4.6\mu\text{m}$. Further data, particularly from *JWST* (Gardner et al. 2006), will be needed to test this hypothesis. Nonetheless, as subdwarfs are rare in a volume-limited census, it is unlikely that this effect is the cause for any other aperture/PRF discrepancies within our sample.

6.3. Visual Inspection

To better understand Classes 0, 1, 2, and 3, we made finder charts for each object that include images from the Digitized Sky Survey 1 and 2 *B*, *R*, and *IR*; the Pan-STARRS1 survey *g*, *r*, *i*, *z*, *y*; the UKIRT Infrared Deep Sky Survey *J*, *H*, and *K* (Lawrence et al. 2007); the UKIRT Hemisphere Survey *J* (Dye et al. 2018); the VISTA Hemisphere Survey *J* and *K_s* (McMahon et al. 2021); the Two Micron All Sky Survey *J*, *H*, and *K_s* (Skrutskie et al. 2006); and *WISE* W1, W2, W3, and W4. These finder charts span a long time baseline and show the background sky at different epochs to see if our target was contaminated by a distant source at the *Spitzer* epochs. We also did a literature search for each object to check for binaries or subdwarfs. This led to the creation of 4 different subclasses: contaminated objects (C), potential binaries (P), known binaries (K), and subdwarfs (S).

6.4. Checking for true and false positives

Once the finder charts were made, it was then possible to search for an estimate of a true and false positive rate for the binary candidates. Although the finder charts provide a starting point for accessing false positives, high-resolution imaging is needed for more fully computing both the true and false positive rates.

To estimate a true positive rate, we searched two high-resolution archives and the literature for known binaries in classes 0 through 3. We searched papers in SIMBAD (Wenger et al. 2000) to find pub-

³ <https://doi.org/10.7910/DVN/SJRXUO>

lished binary systems. The two high-resolution archives we selected are the Keck Observatory Archive (hereafter, KOA; <https://koa.ipac.caltech.edu>) and the *Hubble Space Telescope*/NICMOS image archive studied in [Factor & Kraus \(2022\)](#). The known binary systems found, 12 in total, are listed in Table 5. Comparing this to our K+P+S lists of 72 objects we find an estimated true positive rate of $\sim 17\%$. The true positive rate is likely higher because there are other high-resolution archives that could be searched, and there are some objects that have yet to be observed at high-resolution. This exercise is left for a future paper.

For some of our objects, a real false positive rate is impossible without high-resolution images at the same wavelengths as our *Spitzer* observations, $4.6\mu\text{m}$. Consider a binary T8 (the most abundant spectral type in our sample) and Y1 at a distance of 10pc. Using Figures 16(a) and 16(d) from [Kirkpatrick et al. \(2021\)](#), we find apparent J magnitudes of ~ 18 mag for the T8 and ~ 24 mag for the Y1, and apparent ch2 magnitudes of ~ 13.5 mag for the T8 and ~ 16 mag for the Y1. These values of $\Delta J \approx 6$ mag and $J \approx 24$ mag would make the secondary difficult/impossible to image, even with adaptive-optics imaging from the ground ([Davies & Kasper 2012](#) and [Zhang et al. 2021](#)). However, values of $\Delta \text{ch2} \approx 2.5$ mag and $\text{ch2} \approx 16$ mag are much easier with *Spitzer* or *JWST*.

For earlier type primaries however, a false positive rate can be attempted because observations at $\sim 1\mu\text{m}$ can provide a Δ magnitude sufficient to rule out most secondaries detectable with our technique. Figure 4 of [Gelino et al. \(2011\)](#) shows the contrast ratios achievable for typical high-resolution observations for brown dwarf binary pairs. These ratios depend on the separation between the two objects, the primary’s brightness, and the dynamic range available for secondary detection. The contrast ratios start to plateau at binary separations of $> 0''.2$. Since our ability to detect binaries is limited by the *Spitzer*/IRAC ch2 FWHM of $1''.72$, we can assume this plateau value. It is typical for ground based and NASA/ESA *Hubble Space Telescope* observations to have a depth of ~ 22 mag ([Lowrance et al. 2005](#), [Burgasser et al. 2006](#), and the Keck NIRC2 exposure time calculator⁴). A typical contrast ratio at wide separations is $\Delta H \approx 4$ mag ([Gelino et al. 2011](#)). At our average distance of 15.9pc, an apparent magnitude of $H = 22$ mag would correspond to an absolute H magnitude of 21mag, or a spectral type of Y0 (Figure 16(b) of [Kirkpatrick et al. 2021](#)). A Y0 detection with $\Delta H = 4$ mag is just achievable if the primary has a spectral type of T7.5.

At primary spectral types earlier than this, a companion detectable via our *Spitzer* technique would likely also be detectable via ground based or *Hubble Space Telescope* observations.

In Table 4 the final column, labeled “High-Resolution Imaging”, indicates whether our candidate binary has high-resolution imaging observations in KOA or in [Factor & Kraus \(2022\)](#). There are 25 objects earlier than spectral type T7.5 with high-resolution imaging from these 2 archives. Using these data it is possible to estimate a false-positive rate. We will do this as follows. First, we compare our 25 false binaries to the total number of objects earlier than T7.5 in sub-classes K, P, and S (59) to provide a false positive rate of $\frac{25}{59} = 42\%$. However, there are still 25 objects earlier than T7.5 not in Table 5 and lacking high-resolution imaging in Table 4, so this value is actually a (loose) lower bound for the false-positive rate. Second, we instead compare the same 25 false binaries to the subset of objects earlier than T7.5 with high-resolution imaging observations in Tables 4 and 5. This gives a new false-positive rate of $\frac{25}{34} = 74\%$. However, this is likely an upper bound because the faintest companions to our 25 “false” binaries may not be detectable by our ground-based observations. In reality, we must wait for *JWST* $4.6\mu\text{m}$ imaging to calculate a real false-positive rate, as an object lacking a companion detection at J-band might yet be harboring a cold companion seen only at longer wavelengths.

7. DISCUSSION

7.1. Variability

Figure 10 shows the median of the standard deviation as a function of ch2/W2 magnitude in 0.5-mag intervals. If an object has variability above the line, our analysis would have detected it. For example, if an object has a magnitude of 14.2, no variability can be detected below ~ 12 mmag (1σ) for the *Spitzer* photometry or ~ 60 mmag (1σ) for *WISE* photometry. Points 1 and 2 are known variable objects 2MASS J21392676+0220226 and 2MASS J22282889–4310262 ([Yang et al. 2016](#)), respectively (not included in this study). Number 1 and 2 can be seen to be well above all three lines, which indicates that variability could be found in the unTimely photometry and easily detected in our *Spitzer* photometry. Specifically, for 2MASS J21392676+0220226 we were able to find 14.5% variations in the unTimely W2 photometry, which is different from what is seen in [Yang et al. \(2016\)](#) which found *Spitzer* ch2 peak-to-peak variations of 26%. Furthermore, this plot indicates that the unTimely data will only detect variability if it has relatively large amplitude, while the *Spitzer* data should be able to detect much smaller variations. If we instead

⁴ https://www2.keck.hawaii.edu/inst/nirc2/nirc2_snr_eff.html

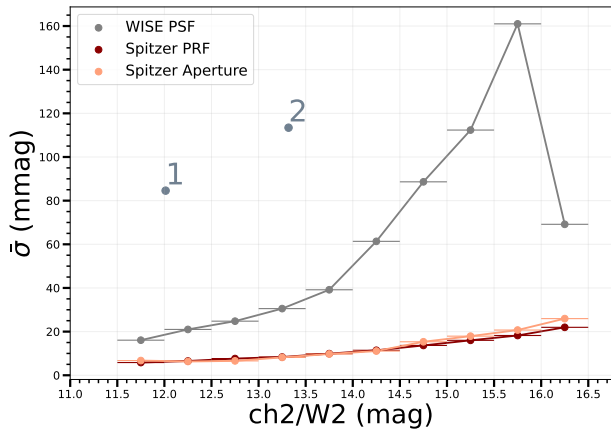


Figure 10. Photometric precision as a function of magnitude. The x-axis shows $ch2_{aperture}$, $ch2_{PRF}$, and $W2_{PSF}$ photometry in 0.5-mag bins, while the y-axis is the median uncertainties between all photometry points (σ) for each bin. Points 1 and 2 are known variables 2MASS J21392676+0220226 and 2MASS J22282889-4310262 (Yang et al. 2016), respectively. The drop in *WISE* sigma at 16-16.5 mag is a result of 4 out of 6 objects in this bin having lower than average standard deviations.

looked at the magnitude percentage variations, we are sensitive to variability of $>4\%$ at 11.5 mag and $>13\%$ at 16 mag, for the unTimely photometry.

This study has shown no variability in brown dwarfs at $\sim 4.6\mu\text{m}$ over a time period of >10 years to the sensitivity limits shown in Figure 10. The large-scale variability to which our survey is sensitive has only been seen in a small number of published objects. This illustrates that large-amplitude variability is rare among brown dwarfs. At smaller amplitudes, however, Yang et al. (2016) found an increase in the percentage of objects with variability near the L/T transition compared to those in the T/Y transition. Figure 2 shows that we have excellent statistics at the T/Y transition, yet we find no large-amplitude variability there.

7.2. Binarity

Brown dwarf binaries are rare and hard to find. Two common ways to find brown dwarf binaries are obtaining a spectrum of a clear spectral composite object (Bardalez Gagliuffi et al. 2014) or visually separating the components via imaging. Our Aperture-PRF technique provides a new way of finding these binaries, in much the same way that the PRF technique alone, through passive deblending, has previously been used to find secondary components (e.g., in circumstellar disks; Martínez & Kraus 2019).

We now compare the MOPEX FWHM of *Spitzer* to the average separation of known nearby brown dwarf binaries, to test our binary hypothesis. The MOPEX

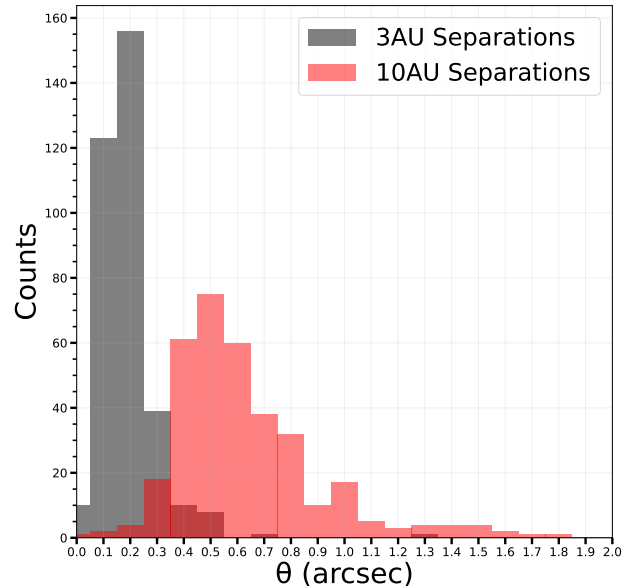


Figure 11. The distribution of angular separation for the 361 objects in our sample assuming a binary with 3 AU physical separation (black) or 10 AU physical separation (red). The 3 AU distribution peaks at $0''.2$ and the one at 10 AU peaks at $0''.5$.

FWHM of *Spitzer* is $1''.72$ at $ch2$ ($4.6\mu\text{m}$). Figure 2 of Burgasser et al. (2007) shows that the average brown dwarf binary has a physical separation between $\sim 3 - 10$ AU. When considering the average distance for our 361 objects is 15.9pc, this leads to an expected separation between $0''.19 - 0''.63$. The distribution of the 361 objects angular separation based on distance assuming 3 and 10AU binary separation can be seen in Figure 11. We see that the objects clump around the predicted separations. However, there are a few objects that are outside of this separation, indicating that they could be angularly separated in the *Spitzer* photometry. Objects of Class 0 must have separation $>1''.72$ in order for the code to passively deblend the object into two different PRF fits. This separation means that Class 0 is very unlikely to have physical binaries. Objects of Class 1, 2, and 3 are only marginally resolved or are within the MOPEX FWHM, meaning that Class 1-3 are the ones most likely to have hidden, faint secondaries.

In Table 2 we show how many objects fall in each class and subclass as defined in §6.1 and §6.3. Details of all 126 objects can be found in Tables 3, 4, and 5. There was only one subdwarf found in this process, 2MASS J06453153-6646120, listed in Table 5 with the known binaries.

We compare known binary/contaminated statistics below for each class:

Table 2. Class/Subclass Statistics

	C	K	P	S	Total
Class 0	10	1	5	0	16
Class 1	3	3	5	0	11
Class 2	18	3	14	0	35
Class 3	23	5	35	1	64
Total	54	12	59	1	126

Reference Codes: (C) Contaminated objects, (K) Known binaries, (P) Potential binaries, and (S) Subdwarfs

- Class 0: Only 1 known binary was found. Most known brown dwarf binaries have separation smaller than the separations at which passive deblending ($1''.33$ to $7''.67$) would take place. Contamination by background objects is the highest among all four classes ($\frac{10}{16} = 63\%$).
- Class 1: This is the highest percentage of known binaries of all four groups ($\frac{3}{11} = 27\%$). The true binaries in this class are likely to have the smallest Δmag and/or largest separations, because they have the most discrepant aperture and PRF-fit measurements. Class 1 also has a significant percentage of background contamination ($\frac{3}{11} = 27\%$).
- Class 2: This class has a much smaller percentage of known binaries ($\frac{3}{35} = 9\%$). True binaries here will likely have slightly larger Δmag and smaller separations. Contamination by background objects is high ($\frac{18}{35} = 51\%$).
- Class 3: This class has the smallest percentage of known binaries ($\frac{5}{64} = 8\%$) and sizable percentage of background contamination ($\frac{23}{64} = 36\%$). Given the smaller difference between aperture and PRF-fit measures, this group is likely to have more spurious binaries than the other classes, but could also have binaries with the tightest separation and/or largest Δmags .

8. CONCLUSION

We examined two $4.6\mu\text{m}$ photometric datasets, *Spitzer*/IRAC ch2 and unTimely W2, to analyze long-term variability in brown dwarfs. Using the *Spitzer*/IRAC ch2 photometry, our study establishes that the typical ch2 variability on ~ 10 year time scales is $< 8\text{mmag}$ for objects at $\text{ch2} = 11.5$ mag and $< 22\text{mmag}$ for objects at $\text{ch2} = 16$ mag. Using the unTimely photometry, which has higher uncertainties than *Spitzer*/IRAC ch2, we find that all variations must be $< 4.5\%$ at 11.5 mag and $< 12.5\%$ at 16 mag. Although a handful of objects in the literature have been

reported with variations greater than this, we conclude that higher-amplitude variability must be the exception rather than the rule.

We also demonstrate a new technique for the identification of brown dwarf binary candidates that uses a comparison of *Spitzer's* aperture and PRF-fit photometry. We present a table of 59 previously unrecognized candidate binaries (Table 4) that constitute prime targets for high-resolution follow-up imaging.

9. ACKNOWLEDGEMENT

This Backyard Worlds research was supported by NASA grant 2017-ADAP17-0067. We thank the Student Astrophysics Society⁵ for providing the resources that enabled the pairing of high school and undergraduate students with practicing astronomers. This work makes use of data products from WISE/NEOWISE, which is a joint project of UCLA and JPL/Caltech, funding by NASA.

Work in this paper is based on observations made with the Spitzer Space Telescope, which is operated by JPL/Caltech, under a contract with NASA. Support for the original parallax work was provided to J.D.K. by NASA through a Cycle 14 award issued by JPL/Caltech. Some data presented here were obtained at the W. M. Keck Observatory, which is operated as a scientific partnership among Caltech, the University of California, and NASA. The authors wish to recognize and acknowledge the very significant cultural role and reverence that the summit of Maunakea has always had within the indigenous Hawaiian community. We are most fortunate to have the opportunity to conduct observations from this mountain. The Observatory was made possible by the generous financial support of the W. M. Keck Foundation. This research has made use of the Keck Observatory Archive (KOA), which is operated by the W. M. Keck Observatory and the NASA Exoplanet Science Institute (NExSci), under contract with the National Aeronautics and Space Administration. This research has made use of the NASA/IPAC Infrared Science Archive, which is funded by the National Aeronautics and Space Administration and operated by the California Institute of Technology. This research has made use of the SIMBAD database, operated at CDS, Strasbourg, France

The Digitized Sky Survey was produced at the Space Telescope Science Institute under U.S. Government grant NAG W-2166. The images of these surveys are based on photographic data obtained using the Oschin

⁵ <https://www.studentastrophysicsociety.com>

Schmidt Telescope on Palomar Mountain and the UK Schmidt Telescope. The plates were processed into the present compressed digital form with the permission of these institutions. Our finder charts also used observations obtained as part of the VISTA Hemisphere Survey, ESO Program, 179.A-2010 (PI: McMahon). The UHS is a partnership between the UK STFC, The University of Hawaii, The University of Arizona, Lockheed Martin and NASA.

The Pan-STARRS1 Surveys (PS1) and the PS1 public science archive have been made possible through contributions by the Institute for Astronomy, the University of Hawaii, the Pan-STARRS Project Office, the Max-Planck Society and its participating institutes, the Max Planck Institute for Astronomy, Heidelberg and the Max

Planck Institute for Extraterrestrial Physics, Garching, The Johns Hopkins University, Durham University, the University of Edinburgh, the Queen's University Belfast, the Harvard-Smithsonian Center for Astrophysics, the Las Cumbres Observatory Global Telescope Network Incorporated, the National Central University of Taiwan, the Space Telescope Science Institute, the National Aeronautics and Space Administration under Grant No. NNX08AR22G issued through the Planetary Science Division of the NASA Science Mission Directorate, the National Science Foundation Grant No. AST-1238877, the University of Maryland, Eotvos Lorand University (ELTE), the Los Alamos National Laboratory, and the Gordon and Betty Moore Foundation.

REFERENCES

- Allers, K. N., Jaffe, D. T., Luhman, K. L., et al. 2007, *ApJ*, 657, 511. doi:10.1086/510845
- Apai, D., Karalidi, T., Marley, M. S., et al. 2017, *Science*, 357, 683. doi:10.1126/science.aam9848
- Artigau, É., Bouchard, S., Doyon, R., et al. 2009, *ApJ*, 701, 1534. doi:10.1088/0004-637X/701/2/1534
- Artigau, É., Lafrenière, D., Doyon, R., et al. 2011, *ApJ*, 739, 48. doi:10.1088/0004-637X/739/1/48
- Artigau, É. 2018, *Handbook of Exoplanets*, 94. doi:10.1007/978-3-319-55333-7_94
- Bailer-Jones, C. A. L. & Mundt, R. 1999, *A&A*, 348, 800
- Bardalez Gagliuffi, D. C., Burgasser, A. J., Gelino, C. R., et al. 2014, *ApJ*, 794, 143. doi:10.1088/0004-637X/794/2/143
- Bardalez Gagliuffi, D. C., Gelino, C. R., & Burgasser, A. J. 2015, *AJ*, 150, 163. doi:10.1088/0004-6256/150/5/163
- Bardalez Gagliuffi, D., Ward-Duong, K., Faherty, J., et al. 2019, *BAAS*, 51, 285
- Beichman, C., Gelino, C. R., Kirkpatrick, J. D., et al. 2013, *ApJ*, 764, 101. doi:10.1088/0004-637X/764/1/101
- Best, W. M. J., Liu, M. C., Magnier, E. A., et al. 2021, *AJ*, 161, 42. doi:10.3847/1538-3881/abc893
- Burgasser, A. J., Kirkpatrick, J. D., Cruz, K. L., et al. 2006, *ApJS*, 166, 585. doi:10.1086/506327
- Burgasser, A. J., Reid, I. N., Siegler, N., et al. 2007, *Protostars and Planets V*, 427
- Burgasser, A. J., Cruz, K. L., Cushing, M., et al. 2010, *ApJ*, 710, 1142. doi:10.1088/0004-637X/710/2/1142
- Cushing, M. C., Hardegree-Ullman, K. K., Trucks, J. L., et al. 2016, *ApJ*, 823, 152. doi:10.3847/0004-637X/823/2/152
- Davies, R. & Kasper, M. 2012, *ARA&A*, 50, 305. doi:10.1146/annurev-astro-081811-125447
- Deacon, N. R., Magnier, E. A., Best, W. M. J., et al. 2017, *MNRAS*, 468, 3499. doi:10.1093/mnras/stx440
- Deming, D., Knutson, H., Kammer, J., et al. 2015, *ApJ*, 805, 132. doi:10.1088/0004-637X/805/2/132
- Ducrot, E., Gillon, M., Delrez, L., et al. 2020, *A&A*, 640, A112. doi:10.1051/0004-6361/201937392
- Dye, S., Lawrence, A., Read, M. A., et al. 2018, *MNRAS*, 473, 5113. doi:10.1093/mnras/stx2622
- Eriksson, S. C., Janson, M., & Calissendorff, P. 2019, *A&A*, 629, A145. doi:10.1051/0004-6361/201935671
- Esplin, T. L., Luhman, K. L., Cushing, M. C., et al. 2016, *ApJ*, 832, 58. doi:10.3847/0004-637X/832/1/58
- Factor, S. M. & Kraus, A. L. 2022, *AJ*, 164, 244. doi:10.3847/1538-3881/ac88d3
- Fazio, G. G., Hora, J. L., Allen, L. E., et al. 2004, *ApJS*, 154, 10. doi:10.1086/422843
- Gardner, J. P., Mather, J. C., Clampin, M., et al. 2006, *SSRv*, 123, 485. doi:10.1007/s11214-006-8315-710.48550/arXiv.astro-ph/0606175
- Ge, H., Zhang, X., Fletcher, L. N., et al. 2019, *AJ*, 157, 89. doi:10.3847/1538-3881/aafba7
- Gelino, C. & Marley, M. 2000, *From Giant Planets to Cool Stars*, 212, 322
- Gelino, C. R., Kirkpatrick, J. D., Cushing, M. C., et al. 2011, *AJ*, 142, 57. doi:10.1088/0004-6256/142/2/57
- Gelino, C. 2012, *Keck Observatory Archive NIRC2*, N099N2L
- Gizis, J. E., Paudel, R. R., Mullan, D., et al. 2017, *ApJ*, 845, 33. doi:10.3847/1538-4357/aa7da0
- Hirst, P. & Cardenes, R. 2016, *Proc. SPIE*, 9913, 99131E. doi:10.1117/12.2231833
- Hora, J. L., Marengo, M., Park, R., et al. 2012, *Proc. SPIE*, 8442, 844239. doi:10.1117/12.926894

- IRSA, 2022, Spitzer Heritage Archive, IPAC, doi:10.26131/IRSA543
- Kellogg, K., Metchev, S., Heinze, A., et al. 2017, *ApJ*, 849, 72. doi:10.3847/1538-4357/aa8e4f
- Kendall, T. R., Jones, H. R. A., Pinfield, D. J., et al. 2007, *MNRAS*, 374, 445. doi:10.1111/j.1365-2966.2006.11026.x
- Kirkpatrick, J. D., Looper, D. L., Burgasser, A. J., et al. 2010, *ApJS*, 190, 100. doi:10.1088/0067-0049/190/1/100
- Kirkpatrick, J. D., Cushing, M. C., Gelino, C. R., et al. 2011, *ApJS*, 197, 19. doi:10.1088/0067-0049/197/2/19
- Kirkpatrick, J. D., Schneider, A., Fajardo-Acosta, S., et al. 2016, *VizieR Online Data Catalog*, *J/ApJ/783/122*
- Kirkpatrick, J. D., Martin, E. C., Smart, R. L., et al. 2019, *ApJS*, 240, 19. doi:10.3847/1538-4365/aaf6af
- Kirkpatrick, J. D., Gelino, C. R., Faherty, J. K., et al. 2021, *ApJS*, 253, 7. doi:10.3847/1538-4365/abd107
- Kolb, U. & Baraffe, I. 1999, *MNRAS*, 309, 1034. doi:10.1046/j.1365-8711.1999.02926.x
- Lang, D. 2014, *AJ*, 147, 108. doi:10.1088/0004-6256/147/5/108
- Lawrence, A., Warren, S. J., Almaini, O., et al. 2007, *MNRAS*, 379, 1599. doi:10.1111/j.1365-2966.2007.12040.x
- Lee, E. K. H., Blečić, J., & Helling, C. 2018, *A&A*, 614, A126. doi:10.1051/0004-6361/201731977
- Leggett, S. K., Cushing, M. C., Hardegree-Ullman, K. K., et al. 2016, *ApJ*, 830, 141. doi:10.3847/0004-637X/830/2/141
- Lépine, S., Rich, R. M., & Shara, M. M. 2003, *ApJL*, 591, L49. doi:10.1086/377069
- Limbach, M. A., Vos, J. M., Winn, J. N., et al. 2021, *ApJL*, 918, L25. doi:10.3847/2041-8213/ac1e2d
- Liu, M. C., Dupuy, T. J., Bowler, B. P., et al. 2012, *ApJ*, 758, 57. doi:10.1088/0004-637X/758/1/57
- Lodieu, N., Allard, F., Rodrigo, C., et al. 2019, *A&A*, 628, A61. doi:10.1051/0004-6361/201935299
- Lowrance, P. J., Becklin, E. E., Schneider, G., et al. 2005, *AJ*, 130, 1845. doi:10.1086/432839
- Luhman, K. L. 2012, *ARA&A*, 50, 65. doi:10.1146/annurev-astro-081811-125528
- Mace, G. N. 2014, *VizieR Online Data Catalog*, *V/144*
- Mainzer, A., Bauer, J., Grav, T., et al. 2011, *ApJ*, 731, 53. doi:10.1088/0004-637X/731/1/53
- Mainzer, A., Bauer, J., Cutri, R. M., et al. 2014, *ApJ*, 792, 30. doi:10.1088/0004-637X/792/1/30
- Makovoz, D. & Marleau, F. R. 2005, *PASP*, 117, 1113. doi:10.1086/432977
- Makovoz, D., Roby, T., Khan, I., et al. 2006, *Proc. SPIE*, 6274, 62740C. doi:10.1117/12.672536
- Marley, M. S., Ackerman, A. S., Cuzzi, J. N., et al. 2013, *Comparative Climatology of Terrestrial Planets*, 367. doi:10.2458/azu_uapress_9780816530595-ch015
- Martinez, R. A. & Kraus, A. L. 2019, *AJ*, 158, 134. doi:10.3847/1538-3881/ab32e6
- Mason, B. D., Wycoff, G. L., Hartkopf, W. I., et al. 2001, *AJ*, 122, 3466. doi:10.1086/323920
- McMahon, R. G., Banerji, M., Gonzalez, E., et al. 2021, *VizieR Online Data Catalog*, *II/367*
- Meisner, A. & Schlafly, E. 2019, *Astrophysics Source Code Library*. ascl:1901.004
- Meisner, A. M., Faherty, J. K., Kirkpatrick, J. D., et al. 2020, *ApJ*, 899, 123. doi:10.3847/1538-4357/aba633
- Meisner, A. M., Schneider, A. C., Burgasser, A. J., et al. 2021, *ApJ*, 915, 120. doi:10.3847/1538-4357/ac013c10.48550/arXiv.2106.01387
- Meisner, A. M., Lang, D., Schlafly, E. F., et al. 2022, arXiv:2204.05748
- Metchev, S. A., Heinze, A., Apai, D., et al. 2015, *ApJ*, 799, 154. doi:10.1088/0004-637X/799/2/154
- Moore, K., Scholz, A., & Jayawardhana, R. 2019, *ApJ*, 872, 159. doi:10.3847/1538-4357/aaff5c
- Müller, T. G., Balog, Z., Nielbock, M., et al. 2016, *A&A*, 588, A109. doi:10.1051/0004-6361/201527371
- Nelson, L. A., Rappaport, S. A., & Joss, P. C. 1986, *ApJ*, 311, 226. doi:10.1086/164767
- Radigan, J., Jayawardhana, R., Lafrenière, D., et al. 2012, *ApJ*, 750, 105. doi:10.1088/0004-637X/750/2/105
- Radigan, J., Lafrenière, D., Jayawardhana, R., et al. 2014a, *ApJ*, 793, 75. doi:10.1088/0004-637X/793/2/75
- Radigan, J. 2014b, *ApJ*, 797, 120. doi:10.1088/0004-637X/797/2/120
- Reach, W. T., Megeath, S. T., Cohen, M., et al. 2005, *PASP*, 117, 978. doi:10.1086/432670
- Reid, I. N., Lewitus, E., Allen, P. R., et al. 2006, *AJ*, 132, 891. doi:10.1086/505626
- Reid, I. N., Cruz, K. L., Burgasser, A. J., et al. 2008, *AJ*, 135, 580. doi:10.1088/0004-6256/135/2/580
- Rowe-Gurney, N., Fletcher, L. N., Orton, G. S., et al. 2021, *Icarus*, 365, 114506. doi:10.1016/j.icarus.2021.114506
- Schlafly, E. F., Finkbeiner, D. P., Jurić, M., et al. 2012, *ApJ*, 756, 158. doi:10.1088/0004-637X/756/2/158
- Schlafly, E. F., Meisner, A. M., & Green, G. M. 2019, *ApJS*, 240, 30. doi:10.3847/1538-4365/aafbea
- Simon, A., Orton, G. S., & Wong, M. H. 2021, *HST Proposal*, 16790
- Skrutskie, M. F., Cutri, R. M., Stiening, R., et al. 2006, *AJ*, 131, 1163. doi:10.1086/498708
- Softich, E., Schneider, A. C., Patience, J., et al. 2022, *ApJL*, 926, L12. doi:10.3847/2041-8213/ac51d8

- Stauffer, J., Marley, M. S., Gizis, J. E., et al. 2016, *AJ*, 152, 142. doi:10.3847/0004-6256/152/5/142
- Tamburo, P., Muirhead, P. S., McCarthy, A. M., et al. 2022, *AJ*, 163, 253. doi:10.3847/1538-3881/ac64aa
- Tannock, M. E., Metchev, S., Heinze, A., et al. 2021, *AJ*, 161, 224. doi:10.3847/1538-3881/abeb67
- Tran, H. D., Mader, J., Conrad, A., et al. 2004, *AAS Meeting Abstracts*
- Tsuji, T. 2005, *ApJ*, 621, 1033. doi:10.1086/427747
- Vos, J. M., Faherty, J. K., Gagné, J., et al. 2022, *ApJ*, 924, 68. doi:10.3847/1538-4357/ac4502
- Wenger, M., Ochsenbein, F., Egret, D., et al. 2000, *A&AS*, 143, 9. doi:10.1051/aas:2000332
- Werner, M. W., Roellig, T. L., Low, F. J., et al. 2004, *ApJS*, 154, 1. doi:10.1086/422992
- Wright, E. L., Eisenhardt, P. R. M., Mainzer, A. K., et al. 2010, *AJ*, 140, 1868. doi:10.1088/0004-6256/140/6/1868
- Yang, H., Apai, D., Marley, M. S., et al. 2016, *ApJ*, 826, 8. doi:10.3847/0004-637X/826/1/8
- Zhang, Z. H., Pinfield, D. J., Gálvez-Ortiz, M. C., et al. 2017, *MNRAS*, 464, 3040. doi:10.1093/mnras/stw2438
- Zhang, J., Cooke, J., Canalizo, G., et al. 2021, *GRB Coordinates Network, Circular Service*, No. 30858, 30858

Table 3. Contaminated Objects

Object Name	RA (deg)	Dec (deg)	Class	Subclass
WISE J004945.61+215120.0	12.439581	21.855476	3	C
2MASSW J0051107-154417	12.79513	-15.73814	2	C
WISEA J005811.69-565332.1	14.54965	-56.892303	3	C
2MASSI J0103320+193536	15.88506	19.593263	3	C
CWISEP J010527.69-783419.3	16.370636	-78.572554	0	C
CWISE J014837.51-104805.6	27.15694	-10.801799	2	C
WISEPA J031325.96+780744.2	48.359129	78.129099	2	C
WISE J032301.86+562558.0	50.75963	56.431894	3	C
WISEPC J033349.34-585618.7	53.457085	-58.939765	3	C
WISE J033515.01+431045.1	53.813599	43.177629	3	C
2MASS J03400942-6724051	55.034396	-67.398518	1	C
2MASS J03582255-4116060	59.594508	-41.267803	2	C
2MASS J04210718-6306022	65.281665	-63.099437	2	C
2MASSI J0443058-320209	70.77379	-32.034919	0	C
PSO J076.7092+52.6087	76.709485	52.608231	0	C
2MASSI J0512063-294954	78.026636	-29.831269	2	C
WISE J052126.29+102528.4	80.360194	10.423512	0	C
CWISEP J063428.10+504925.9	98.618859	50.822681	2	C
WISE J064205.58+410155.5	100.52362	41.031459	3	C
2MASS J07414279-0506464	115.42829	-5.11289	0	C
ULAS J074502.79+233240.3	116.26163	23.54453	0	C
WISE J105130.01-213859.7	162.87537	-21.650142	2	C
SIMP J11322058-3809562	173.08717	-38.166428	3	C
WISE J125715.90+400854.2	194.31615	40.14811	2	C
2MASS J14075361+1241099	211.97158	12.686486	3	C
CWISEP J145837.91+173450.1	224.65736	17.580799	0	C
2MASSI J1526140+204341	231.55718	20.726056	2	C
CWISEP J153859.39+482659.1	234.74805	48.44905	3	C
WISEA J162341.27-740230.4	245.92	-74.04263	2	C
WISE J163940.86-684744.6	249.92274	-68.798677	3	C
PSO J258.2413+06.7612	258.24107	6.761227	1	C
WISEA J173453.90-481357.9	263.72383	-48.233351	2	C
WISEA J173551.56-820900.3	263.96544	-82.150738	3	C
WISE J174102.78-464225.5	265.26168	-46.707965	2	C
WISE J175510.28+180320.2	268.79212	18.056078	3	C
WISE J180952.53-044812.5	272.46884	-4.804453	1	C
WISEA J181849.59-470146.9	274.70665	-47.030892	0	C
CWISE J183207.94-540943.3	278.03261	-54.162757	3	C
WISE J185101.83+593508.6	282.75777	59.586189	3	C
WISE J191915.54+304558.4	289.81597	30.767298	3	C
2MASS J19251275+0700362	291.30355	7.011064	0	C
WISENF J193656.08+040801.2	294.2323	4.131147	2	C
WISE J200050.19+362950.1	300.20898	36.497832	3	C
WISE J201404.13+042408.5	303.51622	4.40277	2	C
WISEA J201833.67-141720.3	304.64037	-14.288602	3	C
2MASS J21265916+7617440	321.76234	76.29985	2	C
2MASS J21543318+5942187	328.637	59.70326	3	C
WISE J223617.59+510551.9	339.07618	51.098434	3	C
WISEP J223937.55+161716.2	339.90682	16.288033	3	C
2MASS J22490917+3205489	342.29281	32.095967	2	C
WISEA J230228.66-713441.7	345.61789	-71.579123	3	C
2MASS J23254530+4251488	351.43842	42.861899	0	C
2MASS J23312378-4718274	352.84951	-47.30787	3	C
2MASSI J2339101+135230	354.79477	13.869448	2	C

Table 4. Potential Binaries

Object Name	RA (deg)	Dec (deg)	Class	Subclass	High-Resolution Imaging ^b
WISE J000517.48+373720.5 ^C	1.3243156	37.622133	3	P	Keck
2MASS J00345157+0523050	8.7173945	5.385477	3	P	Keck
WISE J011154.36-505343.2	17.975789	-50.895856	3	P	
2MASS J01550354+0950003	28.76651	9.832968	0	P	HST
WISEA J020047.29-510521.4	30.197571	-51.089537	3	P	
2MASSW J0205034+125142	31.26636	12.86154	2	P	
WISEA J030237.53-581740.3 ^C	45.656221	-58.294742	3	P	
WISEA J030919.70-501614.2	47.333383	-50.270291	3	P	
2MASS J03101401-2756452	47.55754	-27.946302	2	P	Keck
2MASS J03185403-3421292	49.727839	-34.357738	1	P	HST
SDSSp J033035.13-002534.5	52.64629	-0.42628	3	P	
PSO J052.7214-03.8409	52.72142	-3.84092	3	P	Keck
WISE J033651.90+282628.8	54.216403	28.44105	3	P	
2MASSW J0337036-175807	54.26496	-17.96886	2	P	Keck
WISE J045746.08-020719.2	74.442276	-2.122342	3	P	Keck
2MASS J06020638+4043588	90.528129	40.732372	3	P	Keck
2MASS J07555430-3259589	118.97545	-32.998815	3	P	
SDSS J075840.33+324723.4	119.66821	32.79014	3	P	
WISEPC J075946.98-490454.0 ^C	119.94553	-49.081232	3	P	
WISEA J082640.45-164031.8	126.66664	-16.674235	3	P	Keck
WISEPC J083641.12-185947.2 ^C	129.17153	-18.996518	2	P	Keck
SDSS J085234.90+472035.0	133.14493	47.34106	2	P	Keck
WISEPA J085716.25+560407.6 ^C	134.31581	56.068336	3	P	Keck
SDSSp J085758.45+570851.4	134.4911	57.1464	3	P	
2MASS J09054654+5623117	136.44392	56.38661	0	P	Keck
WISE J092055.40+453856.3	140.23088	45.64886	3	P	
2MASSI J1010148-040649	152.56001	-4.113933	3	P	
2MASSW J1036530-344138	159.22075	-34.696486	2	P	
WISE J103907.73-160002.9 ^C	159.78173	-16.001139	3	P	Keck
2MASS J10430758+2225236	160.7809	22.423186	2	P	HST
2MASS J1104012+195921	166.00555	19.989852	1	P	HST
CFBDS J111807-064016	169.52805	-6.669126	0	P	Keck
WISEP J115013.88+630240.7 ^C	177.56027	63.044022	3	P	Keck
SDSS J115553.86+055957.5	178.97306	5.999081	3	P	Keck
SDSSp J120358.19+001550.3	180.98575	0.26256	1	P	
2MASSI J1213033-043243	183.26275	-4.545563	3	P	HST
SDSS J121951.45+312849.4	184.96319	31.480466	3	P	
2MASS J123147.53+084733.1	187.94283	8.788455	3	P	
PSO J201.0320+19.1072	201.03179	19.106953	2	P	
2MASS J13243559+6358284 ^a	201.14508	63.974268	3	P	
SDSSp J132629.82-003831.5	201.62282	-0.642752	3	P	
WISE J140035.40-385013.5	210.14758	-38.83746	3	P	Keck
SDSS J153453.33+121949.2	233.72292	12.330219	0	P	
PSO J247.3273+03.5932	247.32757	3.592974	3	P	Keck
WISE J165842.56+510335.0	254.67684	51.059217	3	P	Keck
WISE J172134.46+111739.4	260.39341	11.294473	2	P	Keck
WISEA J172907.10-753017.0 ^C	262.27553	-75.505234	3	P	
2MASS J17461199+5034036	266.55258	50.567694	2	P	
WISE J181329.40+283533.3 ^C	273.37128	28.591289	3	P	Keck
2MASS J19010601+4718136	285.27586	47.305732	3	P	Keck
WISE J203042.79+074934.7	307.68001	7.826027	2	P	Keck
WISE J204356.42+622048.9	310.98754	62.347831	1	P	Keck
PSO J319.3102-29.6682	319.31057	-29.668531	3	P	Keck
CWISEP J213249.05+690113.7 ^C	323.20562	69.020736	2	P	
2MASS J21373742+0808463	324.40963	8.146552	1	P	Keck
WISE J214155.85-511853.1	325.48432	-51.31501	2	P	
2MASS J23174712-4838501	349.4483	-48.646791	2	P	
WISEPC J232728.75-273056.5	351.86997	-27.515783	3	P	
2MASS J23440624-0733282	356.02605	-7.5584	0	P	

^a Possible spectral binary (Burgasser et al. 2010)^b Keck: High-resolution imaging from the Keck Observatory Archive (<https://koa.ipac.caltech.edu>), HST: High-resolution imaging from the HST/NICMOS image archive studied in Factor & Kraus (2022)^c Object with spectral type T7.5 or later

Table 5. Known Binaries and Subdwarfs

Object Name	RA (deg)	Dec (deg)	Class	Subclass	Ref
WISE J003110.04+574936.3	7.79433	57.826773	2	K	1
WISEPC J013836.59−032221.2	24.652471	−3.373118	3	K	2
WISEPA J022623.98−021142.8	36.599284	−2.195299	1	K	3
WISEPA J045853.89+643452.9 ^a	74.725621	64.5818	3	K	4
WISEA J064750.85−154616.4	101.96192	−15.77122	0	K	1
PSO J103.0927+41.4601	103.09287	41.460042	2	K	1
WISEPC J121756.91+162640.2 ^a	184.48809	16.443144	1	K	5
SIMP J1619275+031350	244.86502	3.229445	1	K	6
WISEPA J171104.60+350036.8 ^a	257.76888	35.010238	2	K	5
2MASS J21522609+0937575	328.10965	9.633177	3	K	7
PSO J330.3214+32.3686	330.32183	32.368747	3	K	2
2MASS J22551861−5713056	343.82535	−57.2197	3	K	8
2MASS J06453153−6646120	101.36693	−66.76297	3	S	9

^a Object with spectral type T7.5 or later

NOTE—Reference Codes: (1) Best et al. (2021), (2) Unpublished data in the Keck Observatory Archive (<https://koa.ipac.caltech.edu>), (3) Kirkpatrick et al. (2019), (4) Gelino et al. (2011), (5) Liu et al. (2012), (6) Artigau et al. (2011), (7) Reid et al. (2006), (8) Reid et al. (2008), (9) Kirkpatrick et al. (2010)